侧向送丝光纤激光单道熔覆层组织

李凯斌， 李 东， 刘东宇， 于治水
(上海工程技术大学 材料工程学院，上海 201620)

摘 要：采用正交试验法在不锈钢表面侧向送丝单道激光熔覆，确定激光功率、扫描速度、送丝速度对熔覆层横截面几何尺寸、宽高比及稀释率影响，找出最佳工艺参数组合并进行组织分析. 结果表明，当激光功率为2 000 W，扫描速度为4 mm/s，送丝速度为20 mm/s时可得到稳定良好的熔覆层；熔覆层从结合区到表层晶粒形态依次是平面晶、胞状晶、柱状树枝晶、等轴树枝晶、转向树枝晶；熔覆层组织由γ奥氏体和残余δ铁素体组成，δ铁素体主要成蠕虫状、骨架状和侧板条状分布于奥氏体枝晶间或晶界处；熔覆层显微维氏硬度平均值(195 MPa)与基材(207 MPa)相当且分布相对均匀，热影响区维氏硬度略低(178 MPa).

关键词：激光熔覆；侧向送丝；微观组织；显微硬度
中图分类号：TG 142.25 **文献标识码**：A **文章编号**：0253－360X(2014)10－0085－04

0 序 言

不锈钢除具有较好的耐腐蚀性能外，还具有良好的综合力学性能，在航天航空、冶金、石油化工、建筑、机械等领域得到广泛地应用. 由于石油化工、冶金等行业存在有大量高温、腐蚀等恶劣环境条件下承受强烈摩擦磨损作用的零部件，一方面对传统材料提出了更高的性能要求，另一方面也需要一种技术可以快速修复受损的零部件. 激光熔覆技术既可以提高零部件的性能和使用寿命[1,2]，又可以用来修复磨损或有缺陷的零件[3,4]，甚至可以快速成形需要的零件[5,6]，很好的解决了上述问题，得到了国内外的普遍关注和重视.

目前光纤激光器的光电转换效率高达30 %，在加工质量、保养维护及使用成本方面远远优于其它种类的激光器；同时随着激光熔覆技术的发展，送丝激光熔覆相对于送粉熔覆，熔覆材料的利用率高、无粉尘污染，可得到表面平整光滑、内部组织致密的熔覆层[7－9].

结合上述二者优点，文中采用光纤激光器侧向送丝激光熔覆，主要研究激光工艺参数对单道熔覆层横截面几何尺寸等参数的影响，并找出一组最佳工艺组合，进行组织分析和硬度测试，为送丝激光熔覆技术的应用和推广提供指导.

收稿日期：2014－03－17
基金项目：上海市自然科学基金资助项目(11ZR1414600)；上海市教委创新资助项目(11YZ214)

1 试验方法

基材为热轧状态316L不锈钢板，试样尺寸为150 mm×60 mm×15 mm，成分(质量分数，%)为C≤0.03，Si≤1.00，Mn≤2.00，P≤0.045，S≤0.03，16≤Cr≤18，2≤Mo≤3，10≤Ni≤14，余量为Fe. 基材表面熔覆前预先用角磨机去氧化层，并用酒精除污，烘干备用. 熔覆材料选用308L不锈钢焊丝，直径为0.8 mm，成分(质量分数，%)为：C 0.013，Si 0.48，Mn 1.68，P 0.024，S 0.001，Cr 19.57，Mo 0.12，Ni 9.55，Cu 0.13，余量为Fe.

激光熔覆系统主要由IPG YLS-5000光纤激光器、KuKA KR16机器人和KempArc Pulse 450送丝机构组成，激光波长为1 060 nm，焦距为460 mm，最大功率5 000 W，光斑大小为5 mm×5 mm，光斑能量分布均匀. 激光熔覆时离焦量为+6 mm，前向送丝，送丝角度为45 °，氩气保护，后向送气，气体流量为10 L/min. 用KEYENCE Z100超景深显微镜测量熔覆道宽度、高度和深度等参数；用Hitachi S-3400N扫描电镜观察熔覆层微观组织；腐蚀剂用$FeCl_3$盐酸硝酸腐蚀液(含50 mL HCL，10 mL HNO_3，100 mL H_2O，10 g $FeCl_3$)，用PANalytical X'pert PRO型多晶X射线衍射仪分析单道熔覆层组织组成；用HXD-1000TMSC/LCD型显微硬度仪测熔覆层的显微硬度，载荷为0.98 N，保持时间15 s.

试验过程为通过正交试验确定最佳工艺参数组合，分析熔覆层的组织并测定其显微硬度. 采用$L_9(3^4)$正交试验表，其工艺参数设计见表1.

表 1 正交试验工艺参数

Table 1 Orthogonal experiment parameters

工艺编号	激光功率 P/W	扫描速度 v_s/(mm·s^{-1})	送丝速度 v_w/(mm·s^{-1})
1	1 500	2	10
2	1 500	3	15
3	1 500	4	20
4	2 000	2	15
5	2 000	3	20
6	2 000	4	10
7	2 500	2	20
8	2 500	3	10
9	2 500	4	15

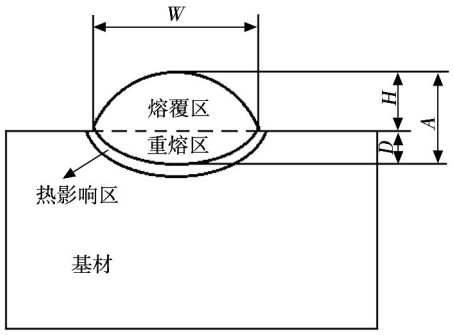

图 1 熔覆道横截面几何尺寸示意图

Fig. 1 Schematic of track cross-sectional geometry

2 试验结果及分析

2.1 工艺参数对熔覆层形貌影响

图 1 为熔覆道横截面几何形貌示意图，主要包括熔宽(W)、熔高(H)、熔深(D)、熔全高 A($A=H+D$)，此外形貌参数还有宽高比 a($a=W/H$) 和稀释率 r($r=D/A$). 宽高比反映熔覆层横向扩展能力，宽高比越大，熔覆层横向扩展能力越强；稀释率反映熔覆层纵向扩展能力及基材对熔覆材料稀释程度，稀释率越小，纵向扩展能力越强，同时基材对熔覆材料稀释程度越低，因此可以用宽高比和稀释率来评价熔覆层三维堆积能力大小.

通过选取正交试验得到的 9 组熔覆层成形稳定区做金相并测量横截面几何尺寸见表 2.

同一因素相同水平激光工艺参数下得到的熔覆层形貌数据取平均值后得表 3. 由表 3 可知，随着激光功率增加，熔高下降，熔宽、熔深、熔全高、宽高比、稀释率都增加；随着扫描速度增加，熔宽、熔高、熔深、熔全高都减少，宽高比增加，稀释率基本不变；随着送丝速度增加，熔宽、熔深略有减少，熔高、熔全高增加，宽高比、稀释率减少.

表 2 正交试验熔覆层形貌数据

Table 2 Orthogonal experiment morphology data of cladding track

工艺编号	熔宽 W/μm	熔高 H/μm	熔深 D/μm	熔全高 A/μm	宽高比 a	稀释率 r(%)
1	3 806.34	934.08	374.88	1 308.96	4.07	28.64
2	3 666.63	1 054.81	127.08	1 181.89	3.48	10.75
3	2 509.91	1 296.27	38.11	1 334.38	1.94	2.86
4	4 854.59	1 067.52	883.22	1 950.74	4.55	45.28
5	4 708.71	1 003.98	501.96	1 505.94	4.69	33.33
6	4 371.96	400.31	540.11	940.42	10.92	57.43
7	5 833.14	1 213.66	1 436.06	2 649.72	4.81	54.20
8	5 585.35	463.90	1 321.90	1 785.80	12.04	74.02
9	5 038.92	527.43	1 156.47	1 683.90	9.55	68.68

表 3 正交试验单因素分析数据

Table 3 Univariate analysis of orthogonal experiment data

单参数平均值后编号	激光功率 P/W	扫描速度 v_s/(mm·s^{-1})	送丝速度 v_w/(mm·s^{-1})	熔宽 W/μm	熔高 H/μm	熔深 D/μm	熔全高 A/μm	宽高比 a	稀释率 r(%)
①	1 500			3 327.63	1 095.05	180.02	1 275.08	3.16	14.08
②	2 000			4 645.09	823.94	641.76	1 465.70	6.72	45.35
③	2 500			5 485.80	735.00	1 304.81	2 039.81	8.80	65.63
④		2		4 831.36	1 071.75	898.05	1 969.81	4.48	42.71
⑤		3		4 653.56	840.90	650.31	1 491.21	6.74	39.37
⑥		4		3 973.60	741.34	578.23	1 319.57	7.47	42.99
⑦			10	4 587.88	599.43	745.63	1 345.06	9.01	53.36
⑧			15	4 520.05	883.25	722.26	1 605.51	5.86	41.57
⑨			20	4 350.59	1 171.30	658.71	1 830.01	3.81	30.13

只考虑增加宽高比，激光功率应取 2 500 W，扫描速度取 4 mm/s，送丝速度取 10 mm/s 进行熔覆；只考虑减少稀释率，则激光功率应取 1 500 W，扫描速度取 3 mm/s，送丝速度取 20 mm/s 进行熔覆. 经验证，两者试验结果都不理想，前者激光功率偏大、送丝过小，造成熔覆层熔高太低、基材稀释过多；后

者激光功率太小,不能在基材上形成稳定熔池,熔覆过程极不稳定. 通过试验调整,P = 2 000 W,v_s = 4 mm/s,v_w = 20 mm/s 时熔覆过程平稳且可获得良好熔覆道见图 2,此时熔覆层形貌参数 W = 4 225.53 μm,H = 889.61 μm,D = 292.28 μm,A = 1 181.89 μm,a = 4.75,r = 24.73%.

图 2　最佳工艺参数组合下熔覆道宏观形貌

Fig. 2　Macroscopic morphology of optimal laser process parameters

2.2　熔覆层微观组织

图 3 所示为激光功率 2 000 W,扫描速度 4 mm/s,送丝速度 20 mm/s 时熔覆层显微组织 SEM 形貌. 由图 3 可知,熔覆层组织细小、致密,与基材成良好冶金结合. 熔覆层由结合区到表层,晶粒形态变化依次为平面晶、胞状晶、柱状树枝晶、等树枝轴晶、转向树枝晶. 熔池底部温度梯度最大,凝固速率最小,首先以无晶核形式直接在基体外延生长出一层平面晶,随着固/液界面的推进,温度梯度减小,凝固速率增大,凝固组织变成胞状晶,当温度梯度减小至某一数值时,凝固组织便从胞晶变成柱状枝晶生长; 由于空气及平行于扫描方向已凝固熔覆层的散热作用,表层金属液在底部枝晶没达到顶部前已沿平行于扫描方向凝固,形成转向树枝晶; 熔覆层表层凝固后,与底部凝固上来的固体包围部分未凝固的金属液,当金属液内部满足成分过冷时开始形核,晶粒向四周生长,形成等轴树枝晶; 基材传热速度最

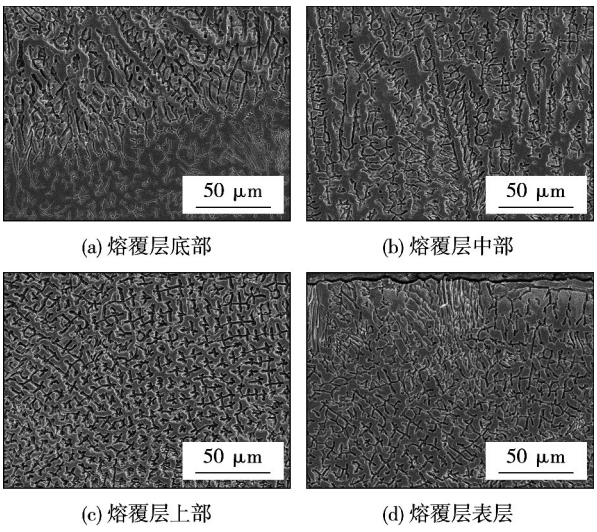

(a) 熔覆层底部　(b) 熔覆层中部

(c) 熔覆层上部　(d) 熔覆层表层

图 3　熔覆层横截面组织形貌

Fig. 3　Microstructure of cross-section of cladding

快,由下往上的凝固速度较大,因此柱状树枝晶占绝大多数.

图 4 为熔覆层和基材的 X 射线衍射结果,两者组织中都存在奥氏体和铁素体. 热轧 316L 不锈钢基材中存在少量铁素体是由于在凝固和热机械加工时铁素体生成元素(主要是 Cr 元素)发生偏聚形成的,而熔覆层中铁素体的存在是其凝固过程造成的. 由图 3 可知,熔覆层中铁素体主要分布在奥氏体枝晶间或晶界处,其形貌为蠕虫状、骨架状和侧板条状,其中蠕虫状或骨架状铁素体主要分布在熔覆层上部和表层,侧板条状铁素体主要分布在熔覆层底部和中部. 凝固模式为典型的铁素体 - 奥氏体模式(F-A),即凝固初始析出相为 δ 铁素体,随着凝固进行及奥氏体生成元素(主要是 Ni 元素)偏聚,在初生 δ 铁素体胞晶界或枝晶间发生包晶/共晶反应形成 γ 奥氏体,奥氏体靠消耗铁素体而不断生长,中等冷却条件下残余 δ 铁素体形貌最终为蠕虫状或骨架状,快速冷却条件下由于铁素体/奥氏体相变时扩散距离减少,侧板条状残余 δ 铁素体替代了骨架状的 δ 铁素体并横切过原始胞状晶或枝状晶生长方向. 因此,熔覆层实际凝固时不同区域冷却速度也不相同.

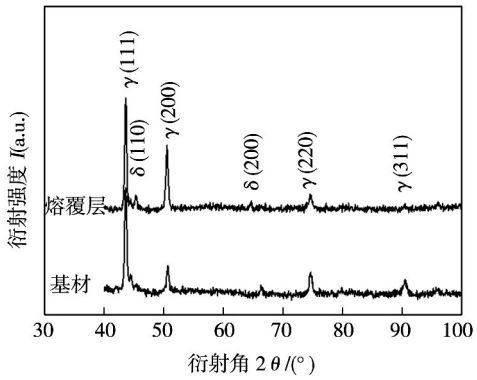

图 4　基材和熔覆层 X 射线衍射结果

Fig. 4　X-ray diffraction results of substrate and cladding

2.3　熔覆层显微硬度

图 5 为熔覆层横截面硬度分布,熔覆层上层等轴枝晶区晶粒细小,柱状枝晶和转向枝晶相对粗大,熔覆层硬度先增加后减小,显微维氏硬度平均值为 195 MPa. 热影响区含铬约 18%、镍 10% ~14%、碳小于 0.1%,其成分大大扩大了 γ 相区并具有稳定奥氏体作用,马氏体转变温度也在室温以下,最终热影响区只有过热区存在,该区域奥氏体晶粒长大,因此维氏硬度平均值偏低为 178 MPa,大致范围为 500 μm. 基材维氏硬度平均值为 207 MPa,比熔覆层略

高，这是因为一方面两者组织状态不同，基材为热轧组织，熔覆层为铸态组织，除高能束加工外，一般热轧组织消除了钢液凝固形成的粗大树枝组织而更细小；另一方面两者成分也不同，316L 不锈钢基材比 308L 不锈钢焊丝除碳含量略高外，钼含量也要高出约 2%，钼除了可以提高钢的耐腐蚀性外，还可以形成碳化物，增加钢的强度，两方面因素下造成基材要比熔覆层硬. 由于激光熔覆层冷却速度快、得到组织细小致密，由图 5 中可看出二者硬度实际差别不大，部分等轴枝晶区熔覆层硬度甚至高于基材. 总体上，从熔覆层到基材硬度过渡平稳，不存在明显软化区.

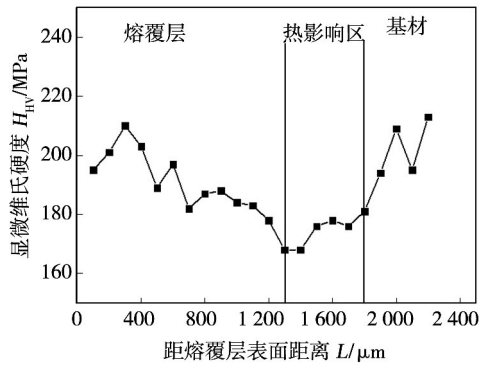

图 5 熔覆层横截面显微硬度分布

Fig. 5 Microhardness distribution of cross-section

3 结 论

(1) 激光工艺参数在一定变化范围内，随着激光功率增加，熔高下降，熔宽、熔深、熔全高、宽高比、稀释率都增加；随着扫描速度增加，熔宽、熔高、熔深、熔全高都减少，宽高比增加，稀释率基本不变；随着送丝速度增加，熔宽、熔深略有减少，熔高、熔全高增加，宽高比、稀释率减少. 得到最佳工艺为激光功率 2 000 W，扫描速度 4 mm/s，送丝速度 20 mm/s.

(2) 熔覆层与基材成良好的冶金结合，组织细小致密、无缺陷. 从结合区到表层晶粒形态变化主要为平面晶、胞状晶、柱状树枝晶、等轴树枝晶、转向树枝晶，其中柱状树枝晶区域占绝大多数. 熔覆层组织为 γ 奥氏体和残余 δ 铁素体，凝固模式为 F-A 模式，δ 铁素体主要成蠕虫状、骨架状和侧板条状分布于奥氏体枝晶间或晶界处，熔覆层凝固时不同区域冷却速度不同.

(3) 熔覆层到基材硬度过渡平稳，无明显软化区. 熔覆层维氏硬度平均值为 195 MPa，与基材的维氏硬度 207 MPa 相当，热影响区维氏硬度偏低为 178 MPa.

参考文献:

[1] Qi Y T, Shi H C, Zou Z D, *et al*. Microstructure and wear behavior of laser claddiig Ni-based alloy composite coatiig reinforced by Ti(C,N) particulates [J]. China Welding, 2008, 17(3): 20 - 23.

[2] 王东生，田宗军，王径文，等. 激光多层熔覆制备厚陶瓷涂层 [J]. 焊接学报，2012，33(5)：57 - 60.
Wang Dongsheng, Tian Zhongjun, Wang Jingwen, *et al*. Experimental on preparation of thick ceramic coating by laser multi-layer cladding [J]. Transactions of the China Welding Institution, 2012, 33(5): 57 - 60.

[3] 范氏红娥，张晓伟，王传琦，等. H13 钢表面 TiC/Co 基激光修复层的显微组织与力学性能 [J]. 焊接学报，2013，34(11)：27 - 31.
Pham Thi Hong Nga, Zhang Xiaowei, Wang Chuanqi, *et al*. Microstructure and mechanical properties of TiC/Co composite coating by laser cladding on H13 steel surface [J]. Transactions of the China Welding Institution, 2013, 34(11): 27 - 31.

[4] Capello E, Colombo D, Previtali B. Repairing of sintered tools using laser cladding by wire [J]. Journal of Materials Processing Technology, 2005, 164/165: 990 - 1000.

[5] 王续跃，王彦飞，江 豪，等. 圆形倾斜薄壁件的激光熔覆成形 [J]. 中国激光，2014，41(1)：0103006-01 - 0103006-06.
Wang Xuyue, Wang Yanfei, Jiang Hao, *et al*. Laser cladding forming of round thin-walled parts with slope angle [J]. Chinese Journal of Laser, 2014, 41(1): 0103006-01 - 0103006-06.

[6] 张凤英，梁广省，张 健，等. 激光多层沉积 Ti-6Al-3Mo 合金的微观组织与性能 [J]. 焊接学报，2013，34(7)：21 - 24.
Zhang Fengying, Liang Guangsheng, Zhang Jian, *et al*. Microstructure and mechanical properties of laser multi-layer deposition of Ti-6Al-3Mo alloy [J]. Transactions of the China Welding Institution, 2013, 34(7): 21 - 24.

[7] Kim J D, Peng Y. Plunging method for Nd: YAG laser cladding with wire feeding [J]. Optics and Lasers in Engineering, 2000, 33(4): 299 - 309.

[8] Capello E, Previtali B. The influence of operator skills, process parameters and materials on clad shape in repair using laser cladding by wire [J]. Journal of Materials Processing Technology, 2006, 174(1/3): 223 - 232.

[9] Abioye T F, Folkes J, Clare A T. A parametric study of Inconel 625 wire laser deposition [J]. Journal of Materials Processing Technology, 2013, 213: 2145 - 2151.

作者简介： 李凯斌，男，1990 年出生，硕士研究生. 主要从事激光熔覆研究. Email: lkbaaa@163.com

通讯作者： 李 东，男，副教授. Email: lid@sues.edu.cn

toughness is closely related to the distribution, pattern and dimension. M-A constituents in the refined zone of welded layers decompose at second peak temperature of 680 ℃, large particle M-A constituents at prior austenite grain boundaries and bulk grain M-A constituents in prior austenite grains are found in the incomplete phase change zone of welded layers at second peak temperature of 820 ℃, and M-A constituents distribute uniformity at 1 050 ℃ with the disappear of prior austenite grain boundaries.

Key words: weld toughness; M-A constituent; refractory steel; incomplete phase transition zone

Chemical reaction of ceramic coatings of Ti-Si-C system on Ti-5Al-2.5Sn substrate prepared by tungsten inert-gas arc cladding YAN Wenqing[1,2], GUI Chibin[2], DAI Le[3] (1. Key Laboratory for Ferrous Metallurgy and Resources Utilization of Ministry of Education, Wuhan University of Science and Technology, Wuhan 430081, China; 2. School of Mechanical and Automotive Engineering, South China University of Technology, Guangzhou 510641, China; 3. Military Representative Office of Navy, Henan Diesel Engine Group Limited Company 407 Factory, Luoyang 471039, China). pp 77 - 80

Abstract: The surface ceramic coatings were prepared on Ti-5Al-2.5Sn substrate by tungsten inert-gas arc depositon process. The microstructures and phases were analyzed using the method of SEM and XRD for the cladding coatings of Ti-SiC and Ti-SiC-C systems. Moreover, the changes of Gibbs energy for possible reactions in systems were calculated using thermodynamic analysis. The results shows that the main microstructure are composed with dendritic TiC and needle-shaped or chrysanthemum Ti_5Si_3 in the cladding coating of Ti-SiC system, the reaction mechanism is $8Ti + 3SiC \rightarrow 3TiC + Ti_5Si_3$. However, in Ti-SiC-C system, there are $TiSi_2$ and Ti_3SiC_2 hybrid microstructure observed besides TiC. $6Ti + 3SiC + C \rightarrow Ti_3SiC_2 + TiSi_2 + 2TiC$ is the main reaction mechanism. In addition, the addition of graphite in Ti-SiC system favors to the generation of self-lubricating Ti_3SiC_2 phases, while the brittle Ti_5Si_3 phases are avoided.

Key words: tungsten inert-gas arc cladding; ceramic coating; reaction mechanism; thermodynamic analysis

Research on scanning path based on metal powder electron beam rapid prototyping CHEN Yunxia[1,2], WANG Xiaojing[3], CHEN Shanben[2], YAO Shun[2] (1. School of Mechanical and Electrical Engineering, Hohai University, Changzhou 213022, China; 2. School of Electronic Information and Electrical Engineering, Shanghai Jiaotong University, Shanghai 200240, China; 3. School of Materials Science and Engineerin, Jiangsu University of Science and Technology, Zhenjiang 212003, China). pp 81 - 84

Abstract: Aimed at the influence of temperature distribution on forming parts caused by scanning paths of filling line of electron beam rapid prototyping technology, finite element model of simultaneous scanning and orderly scanning were established and corresponding experiments were done. The simulation results show that comparing with simultaneous scanning, the forming part quality formed by orderly scanning is better and it can be improved with the offsetting distance shorted. Although with a smaller electron beam current in orderly scanning forming process, the metal powder can also achieved a higher melting temperature and high temperature region, and the forming area is consistent with its scanning area. The equal energy density of each point on the scanning area is help to get relatively smooth forming surface and to easy spread next powder.

Key words: electron beam rapid prototyping; scanning path; energy density; numerical simulation

Microstructure of single track fiber laser cladding with wire feeding by side LI Kaibin, LI Dong, LIU Dongyu, YU Zhishui (School of Material Engineering, Shanghai University of Engineering Science, Shanghai 201620, China). pp 85 - 88

Abstract: Laser cladding was performed on the surface of stainless steel with wire feeding by side. To obtain an optimal combination of process parameters, orthogonal test was used to determine the influences of laser power (P), scanning velocity (v_s) and wire feeding speed (v_w) on the cross-section geometry, aspect ratio and dilution rate of cladding track. The results show that the stable and smooth cladding track can be obtained when the combination of process parameters are $P = 2\ 000$ W, $v_s = 4$ mm/s, and $v_w = 20$ mm/s. Grain morphology of the cladding track from the binding to the surface are planar crystal, cellular crystal, columnar dendrites, equiaxed dendrite, steering dendrites. The microstructure of laser cladding track is composed of γ austenite and residual δ ferrite, and the δ ferrite distributed in the austenite grain boundaries or between dendrites with the vermicular, skeletal and lathy morphologies. The average microhardness of the cladding track is about 195 MPa near to the one of substrate (207 MPa), which is evenly distributed, but the microhardness of heat affected zone (178 MPa) is lower than the one of substrate.

Key words: laser cladding; wire feeding by side; microstructure; microhardness

Numerical simulation and test verification of welding temperature field of 12Cr1MoV heat-resistant steel pipe CHI Luxin, SUN Zhaofan, WU Guangfeng (College of Materials Science and Engineering, Chongqing University of Technology, Chongqing 400050, China). pp 89 - 92

Abstract: To obtain reasonable welding heat input and accurately predict heat affected zone width of 12Cr1MoV heat-resistant steel pipe for controlling boiler welding quality, the thermal circling curves of typical position on steel pipe was obtained by numerical simulation with ANSYS software based on different welding process parameters. Compared the simulation results and the experimental results, it was found that the values calculated of thermal circling curves were close to the ones measured by infrared thermometer. Moverover, the simulation width of welding heat-affected zone was basically the same as the measured value. Welded joint microstructure is mainly acicular ferrite, and heat affected zone microstructure is mainly proeutectoid ferrite and quasi-eutectoid sorbite, while overheated zone have a small amount of ferrite and granular bainite.

Key words: 12Cr1MoV steel; numerical simulation; temperature field; microstructure

Determination of shape parameters of double ellipsoid heat source model in numerical simulation based on SYSWELD software LI Ruiying[1], ZHAO Ming[2], WU Chunmei[1] (1. Department of Physics and Electricity Information Engineering, Daqing Normal University, Daqing 163712, China; 2. College